Journal of Sound and Vibration 329 (2010) 189–201

Contents lists available at ScienceDirect

Journal of Sound and Vibration

journal homepage: www.elsevier.com/locate/jsvi

The evolution of stiction repair for microelectromechanical system cantilevers using periodic excitation

A.A. Savkar [a], K.D. Murphy [b,*]

[a] Department of Mathematics, University of Connecticut, Storrs, CT 06269-3009, USA
[b] Department of Mechanical Engineering, University of Connecticut, Storrs, CT 06269-3139, USA

ARTICLE INFO

Article history:
Received 16 February 2009
Received in revised form
4 August 2009
Accepted 2 September 2009
Handling Editor: M.P. Cartmell
Available online 17 October 2009

ABSTRACT

In some recent experiments, it has been shown that structural vibrations are an efficient means to repair (i.e., unstick) stiction failed microcantilever beams. The analysis that accompanied these experiments identified excitation parameters (amplitude and frequency) that successfully *initiated* the debonding process between the microcantilever and the substrate. That analysis relied on coupling a static fracture model to a vibration model. However, that analysis could not describe what happened *after* the debonding process was initiated. For example, the repair could be partial, where the debonding begins but then arrests—or it could be total, where the beam is returned to its free-standing shape. The present paper examines the *post-initiation* behavior of stiction failed microcantilevers. A new, coupled fracture/vibration model is formulated and used to track the evolution of the repair, in order to determine the extent of the repair under various conditions. Moreover, this model successfully predicts some unusual (but explainable) behavior seen in the previous experiments, regarding partial and complete vibration repair.

1. Introduction

Recent studies conducted on microelectromechanical systems (MEMS) have suggested that sticking failure of individual components within a device is one of the most common and unavoidable reliability issues facing the industry [1,2]. This particular failure mechanism, commonly referred to as stiction, is a significant roadblock preventing the widespread use of microelectromechanical systems in commercial applications. Stiction failures, which are typically driven by surface forces, can be broken down into two categories. The first is fabrication failures. In this case, sticking contact is initiated as material is etched away and the device is *released*. The forces responsible for these failures include (but are not limited to) capillary forces, van der Waals forces, and electrostatic forces [3–5]. The second type of failure occurs after the device is manufactured and has been put into use. These operational failures are referred to as *in-use* stiction. The mechanisms driving these failures are more diverse; dynamic effects may cause components to come into contact, where various forces may lead to adhesive contact. These include the surface forces listed previously, as well as Casimir forces and Coulomb forces [1,6].

Research efforts aimed at improving device reliability at the fabrication stages have taken various tacks. These include introducing novel materials, thin film coatings, smart design changes, and post-fabrication manipulation. For example, during the fabrication of silicon molds for polymer optics, a teflon-like material is used as a coating using a

* Corresponding author.
E-mail address: kdm@engr.uconn.edu (K.D. Murphy).

0022-460X/$ - see front matter © 2009 Elsevier Ltd. All rights reserved.
doi:10.1016/j.jsv.2009.09.003

DRIE (deep reactive ion etching) system. This has been shown to reduce the stiction arising from chemical etching with KOH and IPA [7]. Alkene based monolayer films have been used to produced anti-stiction coatings in microelectromechanical devices [8]. Diamond like carbon coatings have been used to reduce the stiction properties of microsurfaces [9]. Shortly after fabrication (and before being put into operational use), laser pulse heating has been used to repair stiction failed micro-cantilevers [10–12]. This process directs a laser pulse at the failed component. The rapid expansion of the heated component produces thermal strains and causes relative slip between the two mated surfaces, driving decohesion. Although this approach is very attractive, it is still inhibited by the fact that the internal lattice heating can damage the component. This is particularly worrisome for those made out of polymeric and cellular materials, which appear in newer types of microelectromechanical systems devices. Laser induced stress waves have also been considered, as a means to separate stiction failed microelectromechanical systems structures [13,14]. The latter two methods, while showing promise, require a good deal of hardware, setup space as well as easy access to the failed component. As a result, they are reasonable methods for fabrication failures but are considerably less attractive for repairing in-use devices.

For in-use stiction, research has focused on prevention—and not as much on repair. For example, consider RF microelectromechanical systems switches. Common in-use failures modes include a trapped-charge mechanism [15] and break down of the dielectric [16,17]; material solutions for such problems have dominated. Self-assembled monolayers (SAM) [18] have significantly reduced the release and in-use stiction, as compared to plasma deposited fluorocarbons. Designers have also proposed avoiding stiction by redesigns: by limiting the length of free standing cantilever beams stiction may be avoided during the operation of certain actuators [6]. Additional features, such as sidewall spacers and bumps, may be etched into the device and help reduce the contact area of the neighboring surfaces, thereby reducing the potential for stiction [19]. These design approaches have met with some success, though they limit design flexibility.

Recently, it has been shown that structural vibrations may be used as an effective alternative for the repair of stiction failed components [20,21]. The benefit to this approach is that electrical actuation pads may be built into the substrate of a microelectromechanical systems chip and used to deliver a periodic electrical potential, driving the structural vibrations. In short, the built-in functionality of the chip may be used to used to effect the desired repair. The physical process behind this approach can be seen schematically in Fig. 1. This shows a microcantilever stuck to a substrate. At the right end of the unstuck section, $x = s$, the beam and the substrate merge and form a singularity, which is geometrically similar to a crack tip. As the unstuck portion of the beam is driven, lateral vibrations are induced and the crack may or may not advance; the onset of crack propagation (also referred to as debonding or peeling, in this physical context) and its continued growth may be described via dynamic fracture mechanics. The preliminary work on this approach considered a beam with a fixed unstuck length, i.e., $s = \text{constant}$. Parameter combinations of the forcing amplitude and frequency (F, Ω) that *initiated* peeling were then obtained [20]. The present study differs in several ways—but the most dramatic difference is that the unstuck length is now a function of time, $s = s(t)$. As such, the evolution of the stiction repair process may be described. As an aside, it may be noted that because the domain of the problem is restricted to the unstuck portion of the beam (which changes with time), this problem constitutes a moving boundary problem.

The model developed here uses assumed modes (for spatial discretization) along with Lagrange's equations to describe the lateral deformation of the unstuck portion, $w(x,t)$, and the growth of the unstuck portion, $s(t)$. This formulation incorporates inertial effects into Griffith's criterion for mode I fracture [22,23]. Finally, the limitations of this model should be clearly stated. This model may be used to examine growth of the unstuck region (i.e., crack growth). In other words, this model remains valid only for an advancing crack, $\dot{s} \geq 0$. The complex contact (and possibly re-adhesion) mechanics of crack closure are not considered here. A simple model for static crack closure has been proposed elsewhere [24,25]. The issue of dynamic crack closure is not addressed in this work. This is not to suggest that such behavior is either impossible or irrelevant—quite the contrary. The intent here is to focus only on the crack advance scenario; this has the dual advantage of simplifying both the analysis and the interpretation of the response (making it easier to connect response behavior to features in the model).

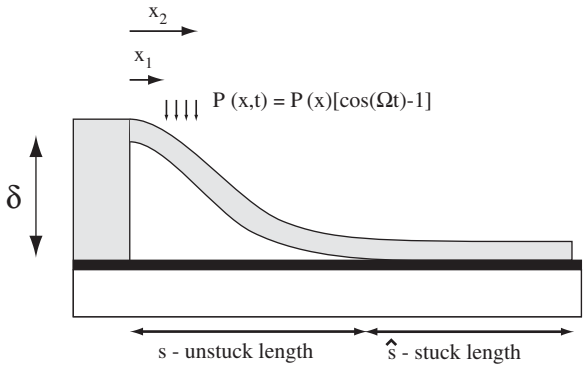

Fig. 1. A schematic of a micro-cantilever stuck to a substrate. Its unstuck length is s. A periodic harmonic load is applied over a small portion of the beam, in an attempt to unstick it.

The analytic model, presented in Section 2, captures all of the relevant mechanics and leads to a set of governing ODEs describing the response of the system. Since the ODEs are nonlinear and coupled, a numerical solution is sought. The solution procedure is outlined in Section 3, and some potential numerical difficulties are identified. Results are presented in Section 4; this begins with some validation cases and then shows the impact of the excitation frequency and amplitude on the response. Lastly, the frequency is swept, as was done in the experiments of Ref. [20]. Interestingly, the model results demonstrate phenomenologically similar behavior to the experiments: increasing frequency sweeps result in partial repair while decreasing sweeps produce more complete repair. The mechanism responsible for this is explained in terms of the underlying physics.

2. Analytical model

The system under consideration is the s-shaped, stiction failed micro-cantilever, shown in Fig. 1. The model will describe behavior only in the unstuck portion of the beam, $x \in [0, s]$. The beam is a homogeneous, linear Euler–Bernoulli beam with an unstuck length of s, total length of L, thickness h, and depth b. The left end is clamped at a distance δ above the substrate. The typical dimensions of the beams used were $L = 1000\,\mu\text{m}$, $s = 0.5\,\text{L}$, $h = 2\,\mu\text{m}$, $\delta = 2\,\mu\text{m}$. The Young's modulus used was $E = 160\,\text{GPa}$. The right end of the unstuck portion of the beam (at $x = s$) has a fixed displacement $w(s,t) = \delta$ and no slope. A distributed load is used to represent the electrical loading used in the preliminary experiments [20]. Of course, an electric lateral load will be gap dependent and, as the beam vibrates, this load will change. However, if the actuation pad used for exciting the beam is placed close to the left post (as in the experiments of reference [20]), the lateral deflection will be small and the gap size will be roughly constant. Alternatively, one may deliver the load using an instrumented nano-indenter eliminating any gap dependency in the load. It is this scenario that we consider here. The load may be expressed as

$$P(x,t) = P(x)[\cos(\Omega t) - 1]. \tag{1}$$

This consists of a static downward load and a periodic load. This excitation is consistent with the fact that upward forces are difficult to apply (note that the load never exceeds zero). In addition, the time-varying portion of this load gradually lifts off from zero (with zero slope at $t = 0$), as would most realistic loadings.

The total lateral beam deflection $w(x,t)$ is measured from the free-standing configuration and consists of two parts. The first represents the no-load equilibrium position of the adhered beam, i.e., describing the s-shape. This deflection is given by $w_s(x,t)$ and may be obtained by elementary beam theory with the boundary conditions: $w_s(0,t) = 0$, $w_s'(0,t) = 0$, $w_s(s,t) = \delta$, and $w_s'(s,t) = 0$, where primes denote differentiation with respect to x. The result is

$$w_s(x,t) = \delta\left[\frac{3x^2}{s(t)^2} - \frac{2x^3}{s(t)^3}\right]. \tag{2}$$

This is an s-shaped beam, whose lateral deformation (w_s) will clearly evolve as the beam unpeels from the substrate as $s(t)$ increases. In addition to these lateral shape changes due to unpeeling, there can be lateral deformations due to the applied external load. These are additional deformations that occur about the s-shape. Hence, it is assumed that the total deflection function has the form: $w(x,t) = w_s(x,t) + w_m(x,t)$.

Assuming the response is dominated by a single mode, the vibration response may be expressed as

$$w_m(x,t) = A(t)\Psi_1\left(\frac{x}{s(t)}\right). \tag{3}$$

Here, A is the time dependent first mode amplitude and Ψ_1 is the first clamped–clamped vibration mode shape. Of course, the mode shape is also time dependent, since it depends on the unstuck length. This is given by

$$\Psi_1(x,t) = 0.5[\delta_1\, e^{(\beta_1 x/s(t))} + \gamma_1\, e^{(-\beta_1 x/s(t))}] - \cos\left(\frac{\beta_1 x}{s(t)}\right) - \alpha_1 \sin\left(\frac{\beta_1 x}{s(t)}\right), \tag{4}$$

where $\beta_1 \approx 4.73$, $\alpha_1 \approx 0.9825$, $\delta_1 = 1 - \alpha_1$, and $\gamma_1 = 1 + \alpha_1$ [26]. As stated previously, the total deflection is

$$w(x,t) = w_s(x,t) + w_m(x,t). \tag{5}$$

The two generalized coordinates in this problem are the unstuck length $s(t)$ and the modal amplitude $A(t)$. The objective is to use Lagrange's equations to obtain equations that will govern the behavior of s and A. This is accomplished by writing expressions for the kinetic (T) and strain energy (U):

$$T = \frac{1}{2}\int_0^{s(t)} \rho A_r(\dot{w})^2\, dx \tag{6}$$

and

$$U = \frac{1}{2}\int_0^{s(t)} EI(w'')^2\, dx, \tag{7}$$

where ρ is the material density, A_r is the cross sectional area, E is the Young's modulus, I is the area moment of inertia of the beam, and dots and primes refer to differentiation with respect to time and space, respectively. In this case, w is the total

deflection, given by Eq. (5) (using Eqs. (2) and (3)). The Lagrangian is simply

$$\mathcal{L} = T - U. \tag{8}$$

At this point, one might be tempted to use Lagrange's equation straightaway. However, it is not clear that the standard form of Lagrange's equations are valid; to arrive at Lagrange's equations, Hamilton's principle is used along with integration by parts. But here one of the unknown variables appears in the limits of the spatial integrals (Eqs. (6) and (7)), preventing the direct application of integration by parts. The remedy to this problem is presented in Ref. [27] and, interestingly, the standard form of Lagrange's equation remain valid:

$$\frac{\mathrm{d}}{\mathrm{d}t}\left(\frac{\partial \mathcal{L}}{\partial \dot{s}}\right) - \frac{\partial \mathcal{L}}{\partial s} = Q_s \tag{9}$$

and

$$\frac{\mathrm{d}}{\mathrm{d}t}\left(\frac{\partial \mathcal{L}}{\partial \dot{A}}\right) - \frac{\partial \mathcal{L}}{\partial A} = Q_A, \tag{10}$$

where Q_s and Q_A are the generalized forces. These arise from the externally applied load and the dissipation that occurs at the crack tip, as new surface area is being formed. Let us first consider the work done due to the applied force. The work is given by

$$\int_0^s W = \int_0^s F \cdot w(x,t). \tag{11}$$

To find the generalized forces one needs to take the variation of the work W with respect to the generalized coordinates s and A, which is given by

$$\int_0^s \delta W = \int_0^s \underbrace{\left(F\frac{\partial w}{\partial s}\right)}\delta s + \int_0^s \underbrace{\left(F\frac{\partial w}{\partial A}\right)}\delta A. \tag{12}$$

First term under the bracket is Q_{s1} the generalized force due to the applied load. This contributes to the longitudinal displacement and is given by

$$Q_{s1} = P[1-\cos(\Omega t)]\left(\frac{\delta}{2} + 0.408A\right). \tag{13}$$

The second term under the bracket is Q_A the generalized force due to the applied load. This contributes to the transverse displacement and is given by

$$Q_A = P[1-\cos(\Omega t)](0.408s). \tag{14}$$

The constant term (0.408) is obtained from integration of the shape function $\Psi_1(x,t)$ over the entire span of the unstuck length s of the beam.

Now consider the work done at the crack tip as new surfaces are created (and the interface energy Γ is overcome). This work W_G is determined from the energy release rate G. This is obtained by taking the variation of work W_G with respect to s and is given by

$$Q_{s2} = \frac{\partial W_G}{\partial s}\delta s = \frac{-18EI\delta^2}{s_0^4} = -G. \tag{15}$$

It should be noted that this work is done when the crack growth is impending and the crack tip velocity, $\dot{s}$, is zero. Expressions for Q_A and $Q_s = Q_{s1} + Q_{s2}$ along with Eqs. (6) and (7), Lagrange equations may be used. This produces two coupled, nonlinear ODEs in the unknowns s and A. These have the form

$$(C_1 + C_2A^2 + C_3\delta A)\frac{\ddot{s}}{s} + (C_4A - C_5)\ddot{A} = (\kappa_1 + \kappa_2 + \kappa_3 + \kappa_4 + Q_s), \tag{16}$$

where

$$\kappa_1 = C_5\dot{A}^2, \tag{17a}$$

$$\kappa_2 = (C_7A^2 + C_8A + C_9)\frac{\dot{s}^2}{s}, \tag{17b}$$

$$\kappa_3 = -(C_{10}A + C_{11})\frac{\dot{A}\dot{s}}{s}, \tag{17c}$$

$$\kappa_4 = \frac{P_1A}{s^4} + \frac{P_2}{s^4} + \frac{P_3A^3}{s^4} \tag{17d}$$

and

$$(P_4A - P_5)\ddot{s} + P_6 s\ddot{A} = (\varphi_1 + \varphi_2 + \varphi_3 + Q_A), \tag{18}$$

where

$$\varphi_1 = (P_7A - P_8)\frac{\dot{s}^2}{s}, \tag{19a}$$

$$\varphi_2 = (P_9)\dot{A}\dot{s}, \tag{19b}$$

$$\varphi_3 = \frac{-P_{10}A}{s^3} - \frac{P_{11}}{s^3}, \tag{19c}$$

where $C_1 \rightarrow C_{11}$, and $P_1 \rightarrow P_{11}$, are constants which arise out of the analysis. The values of these constants have been provided in the appendix of this paper. It should be noted that these coupled nonlinear ODEs have multiple terms involving A and s on the right-hand side. To facilitate easy reading of these terms, each of the terms on the right-hand side of the two equations, is represented by $\kappa_1 \rightarrow \kappa_4$ in Eq. (16), and by $\varphi_1 \rightarrow \varphi_3$ in Eq. (18). Eq. (17), and Eq. (19), illustrate the individual terms on the right-hand side of the governing equations.

These equations, governing the evolution of A and s, are coupled, nonlinear ODEs. A general, closed-form solution to these equations does not exist. Moreover, a local linearization is not physically meaningful, as the unstuck length may grow considerably. The following section discusses the numerical procedure used to obtain solutions to these equations.

3. Numerical formulation

A traditional time marching approach is used to obtain a solution to the governing equations. This requires that the equations be re-cast first into a order form; this converts the two, second-order equations into four, first-order ODEs in the variables A, $\dot{A}$, s, and $\dot{s}$. Once in this form, a simple fourth-order Rung–Kutta was used [28]. Throughout every simulation, the sign of $\dot{s}$ was constantly monitored; if $\dot{s} < 0$, the model would no longer be valid and the simulation was stopped.

It should also be noted that a more sophisticated solver was used initially. A stiff equation solver was used because it was thought that the rate of debonding $\dot{s}$ might be many orders of magnitude larger than the lateral speed $\dot{A}$, potentially rendering the system stiff. However, for the geometries and materials considered in this work, the equations never exhibited numerical instabilities due to stiffness. Hence, a simple Runge–Kutta scheme was used throughout.

4. Results

The response characteristics of this system are considered piecemeal—in an attempt to build-up our physical understanding of the system. To begin, the free response is considered. Here, the externally applied dynamic load is removed and the beam is initially pre-compressed so that it will immediately begin to peel off. Inertial effects dominate. Then the excitation is turned on and the importance of the lateral vibrations ($A(t)$) are highlighted. Next, the role of the excitation level and frequency on the repair process is examined. Finally, frequency sweeps and frequency tracking are carried out in order to determine whether these are more effective repair approaches (and to confirm certain behaviors seen experimentally).

4.1. No load analysis—transient behavior

As described in Section 2, $w_m(x,t)$ is the lateral response to external excitation and is super-posed on the s-shape $w_s(x,t)$. As such, in the absence of external excitation, it is presumed that $w_m(x,t) = 0$. This assumption is similar to that made in Ref. [22], where transverse deflections of a cracked specimen are ignored. In this case, the kinetic and the potential energies simplify to

$$T_{\text{tot}} = \frac{18}{105}\frac{\rho A_r \delta^2 \ddot{s}}{s} \tag{20}$$

and

$$U_{\text{tot}} = \frac{6EI\delta^2}{s^3}. \tag{21}$$

These energies are then used in Eq. (9), to obtain the equation governing $s(t)$:

$$\ddot{s} = \frac{\dot{s}^2}{2s(t)} + \frac{105}{2}\frac{EI}{\rho A_r}\frac{1}{s(t)^4} - G\left[\frac{105}{36}\frac{1}{\rho A_r \delta^2}\right]. \tag{22}$$

To initiate motion, the beam is initially pre-compressed into the substrate and held there; this is accomplished by setting the initial conditions to $s(0) = s_0$ and $\dot{s}(0) = 0$. Note that $s = s_0$ is defined as the static equilibrium position for a system with an interface energy of Γ. Hence, to arrive at true pre-compression (where the beam will immediately start to un-peel), the

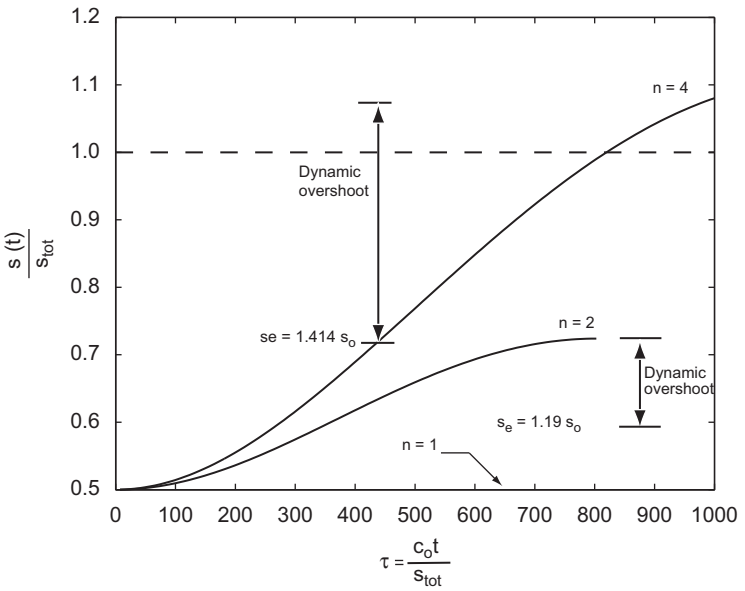

Fig. 2. A plot of non-dimensional beam length versus non-dimensional time for various values of bluntness parameter n. $s_0 = 500\,\mu\text{m}$, $s_{\text{tot}} = 1000\,\mu\text{m}$.

interface energy must be set to $n\Gamma$, where $n>1$. In this case, the static equilibrium position is obtained by setting the energy release rate equal to the new interface energy: $18EI\delta^2/s^4 = n\Gamma$. Solving for the static equilibrium position gives $s_{\text{eq}} = \sqrt[4]{n\Gamma\delta^2/18EI} = \sqrt[4]{n}s_0$. This can also be used to simplify Eq. (22), which becomes

$$\ddot{s} = \frac{\dot{s}^2}{2s(t)} + \frac{105}{2}\frac{EI}{\rho A_r}\left[\frac{1}{s(t)^3} - \frac{s(t)}{ns_0^4}\right]. \tag{23}$$

Fig. 2 shows the growth in the unstuck length, s, for three cases: $n = 1, 2$, and 4. The unstuck length s is normalized by the total beam length s_{tot}. The primary motivation behind using the s_{tot} which is the total length of the beam is due to the fact that we are looking at the peeling process of the beam from its original unstuck length s. Thus when $s/s_{\text{tot}} = 1$ we can see that beam is completely peeled off or is in the tip stuck mode. For the three cases in the figure the equilibria are at $s = s_0$, $1.189s_0$, and $1.414s_0$, respectively. For the case $n = 1$, the beam is not pre-compressed and the beam starts off at its equilibrium position. As a result, the crack does not advance. For $n = 2$, beam is pre-compressed when at $s = s_0$. When released, the unstuck length quickly grows past its equilibrium position of $s_e = 1.189s_0$ and arrests near $s(t)/s_{\text{tot}} = 0.705$, when $\dot{s} = 0$. This dynamic overshoot—past its equilibrium position—is driven purely by inertial effects. This dynamic overshoot can be understood by looking at Eq. (23). Initially, the term in the parentheses on the right-hand side is positive for any $n>1$ and $\dot{s}(0) = 0$. The beam therefore accelerates from its initial position. As it does, the term in the parentheses on the right-hand side decreases while the first term increases. This situation persists until the term in parentheses becomes sufficiently negative to override the positive contribution from the first term and causes the beam (crack) tip to decelerate. The numerical simulation is stopped when the crack velocity $\dot{s}$ becomes zero indicating crack arrest. Similarly, for $n = 4$, the beam is precompressed to s_0 and released. The beam quickly peels off of the substrate, past its equilibrium length of $s_e = 1.414s_0$, and arrests near $s(t)/s_{\text{tot}} = 1.1$. Of course, once $s(t)/s_{\text{tot}} > 1$ the beam has de-bonded from the substrate and is stuck only at its tip; this is referred to as being "tip stuck" or "arc shaped" (not s-shaped). Because of the geometry change, a sharp crack tip no longer exists and, therefore, the model is no longer valid. Consequently, this model is only valid up to (but not including) $s/s_{\text{tot}} = 1$ and cannot predict complete repair, i.e., a return to the freestanding shape. Of course, once the arc-shape (i.e., the right end of the beam (the free end) just comes in contact with the substrate) has been attained, inertial effects could force the beam tip to de-bond, popping the beam free. But this is beyond the scope of the present model. For the remainder of this text, the term *complete repair* will be used synonymously with the condition $s/s_{\text{tot}} = 1$, although this is not strictly correct.

These results clearly indicate the importance of inertia in these dynamics problem; had the inertia been neglected, the system would have unpeeled to the equilibrium value s_e and stopped. But clearly the inertia causes considerable overshoot and, for the case of $n = 4$, it was enough to effect a "complete repair".

4.2. The influence of harmonic excitation

The previous result is essential to understand the basic mechanics of the problem without involving the complication of the added harmonic load. The harmonic loading is now re-introduced.

4.2.1. The importance of lateral vibrations

Ultimately, the objective is to characterize the growth of the unstuck region under periodic loading. In other words, $s(t)$ is the quantity of interest. So one might rightly ask whether lateral vibrations play an important role. Moreover, in the traditional double cantilever dynamic fracture literature (with static loads), lateral vibrations are uniformly neglected [22]. And so it is important to determine whether lateral vibrations are relevant to the underlying debonding process.

To answer this question, two different simulations were carried out. The first case integrated equations (16) and (18), simultaneously, with the modal amplitude and its derivatives are set to zero ($A = \dot{A} = \ddot{A} = 0$), such that lateral vibrations were completely ignored. The second case put no stipulations on the modal amplitude or its derivatives thus incorporating w_m in the response. All the material properties and geometry remain the same as in the last section. Here the interface energy is $\Gamma(n = 1)$. The force amplitude was $P = 2000\,\mu\text{N}$ and the excitation frequency was $\Omega/\omega_1 = 0.9$, where ω_1 is the first natural frequency of the beam in its initial shape. Fig. 3 shows the growth of the unstuck region for these two cases. The first case (Fig. 3a) shows that the beam unpeels to a final unstuck length of approximately $s/s_{\text{tot}} = 0.65$ before it arrests. This represents a 30% change in the unstuck length. The second case (Fig. 3b) shows that the unstuck length grows to approximately $s/s_{\text{tot}} = 0.85$ for the same excitation parameters. This represents a 65% repair. From this one simple case, the conclusion is obvious: lateral oscillations can have a tremendous impact on the extent of the repair and should not be dismissed out of hand.

4.2.2. Effects of the forcing amplitude and forcing frequency

In Ref. [20], it was shown that the forcing amplitude and frequency dramatically influenced whether the debonding process was initiated or not. In that study, it was shown that if the excitation frequency was near a resonant frequency, debond initiation was much more likely. Likewise, it is important to see how these quantities impact the debonding process after initiation.

The material properties and beam geometry are the same as in the previous case. To examine the impact of the excitation amplitude only, the excitation frequency is held fixed at $\Omega/\omega_1 = 0.9$, where ω_1 is the first natural frequency of the system at its initial unstuck length, s_0. However, it should be noted that this is *not truly* a fixed frequency problem. As the unstuck region grows, the effective length of the beam (i.e., its free length) grows, which reduces the natural frequency. So even though the driving frequency Ω is fixed, its proximity to the resonance condition changes. But a fixed Ω is physically easy to realize and, hence, of practical importance. Frequency tracking, where the frequency ratio Ω/ω_1 is held fixed, is discussed in Section 4.2.4.

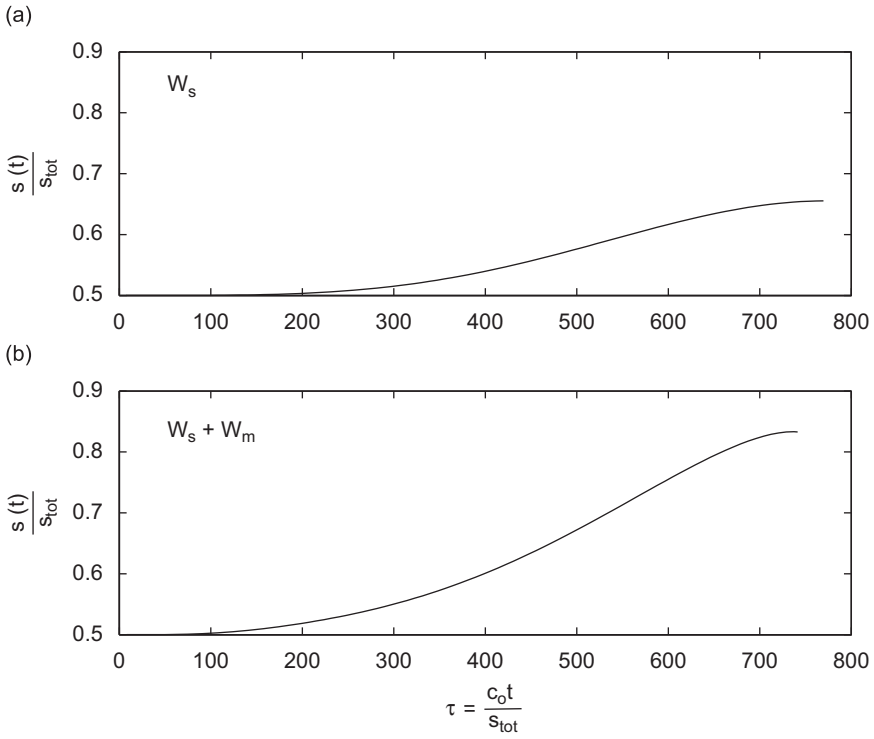

Fig. 3. A plot of non-dimensional beam length versus non-dimensional time for a fixed force value. $s_0 = 500\,\mu\text{m}$, $s_{\text{tot}} = 1000\,\mu\text{m}$: (a) without modal amplitude and (b) with modal amplitude.

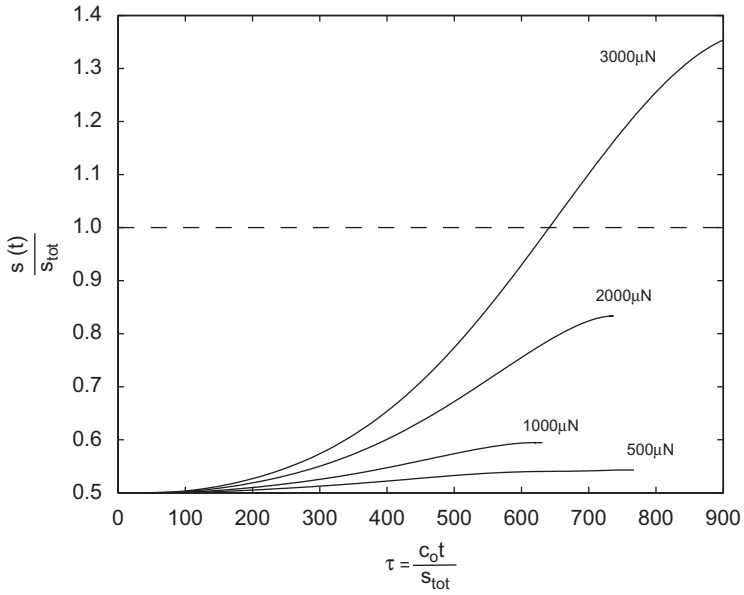

Fig. 4. A plot of non-dimensional beam length versus non-dimensional time showing the effect of various force values for a fixed excitation frequency. $s_0 = 500\,\mu m$, $s_{tot} = 1000\,\mu m$.

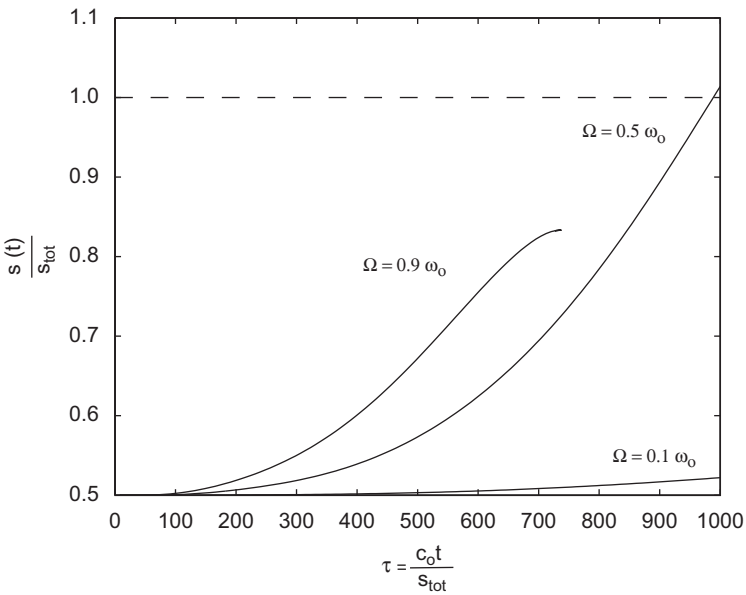

Fig. 5. A plot of non-dimensional beam length versus non-dimensional time showing the effect of variation of excitation frequency for a fixed force value. $s_0 = 500\,\mu m$, $s_{tot} = 1000\,\mu m$.

Fig. 4 shows the growth of the unstuck region as a function of time for various excitation amplitudes. These show a monotonic increase in the final unstuck length as the excitation amplitude is increased. At 2000 μN, the unstuck length grows to approximately $s = 0.85 s_{tot}$, which represents a 65% repair. At 3000 μN, the repair has proceed to complete repair. It is also interesting to note that the debonding process arrests at different times. The time to arrest decreases from 500 to 1000 μN. But it increases from 1000 to 2000 μN. It is difficult to explain this behavior in terms of a particular physical feature of the system, since the response characteristics of the system are also changing dynamically.

Now consider the impact of the excitation frequency. Here the same physical system is used and the excitation amplitude is fixed at $P = 2200\,\mu N$. Fig. 5 shows how the unstuck region grows as a function of time. If the beam is driven well below the first resonance $\Omega = 0.1\omega_1$ (again, ω_1 is the initial natural frequency of the beam, at $s = s_0$), the unstuck

length grows slightly to $s = 0.55 s_{tot}$ but then arrests. If the excitation frequency is increased to $\Omega = 0.5\omega_1$, the beam is repaired. If the excitation frequency is increased still further to $\Omega = 0.9\omega_1$, the unstuck length grows to $0.85 s_{tot}$ and then arrests, short of full repair. This result may seem unusual. Driving the system closer to (the initial) resonance actually produces less repair than driving it at half of the (initial) resonance. This may be explained as follows. For $\Omega = 0.9\omega_1$, the excitation is initially sub-resonant (though nearly resonant) and debonding begins immediately with a large velocity. However, as the beam unsticks, the natural frequency drops and passes through the excitation frequency. The excitation frequency very quickly becomes super-resonant ($\Omega \gg \omega_1$), reducing the steady-state vibration amplitude. This causes the system to arrest. But, for the case $\Omega = 0.5\omega_1$, the situation is different. Debonding is initiated and, again, the natural frequency drops. But it takes longer for the natural frequency to coincide with the excitation frequency. This permits more momentum to build, such that the debonding process may be carried through to completion. For the case $\Omega = 0.1\omega_1$, not enough momentum ever builds up, the unstuck grows slightly and the natural frequency drops slightly—but not enough to ever coincide with the excitation frequency. This prevents a resonance condition and leads to a very modest repair.

4.2.3. *Effect of a frequency sweep*

Frequency sweeps refer to increasing or decreasing the excitation frequency at a prescribed rate. Preliminary experiments have used frequency sweeps and shown that the extent of a repair depends on the direction of the sweep [20]. This directional dependence could not be explained previously as the model only looked at the parameters that *initiated* stick release. The current analytical model is capable of capturing this phenomenon and explaining the underlying physics of such an occurrence. Fig. 6 shows two curves. The first curve indicates the length of the unstuck beam when the excitation frequency is swept up. Here the frequency was swept up over the range, $0.1\omega_1 \rightarrow \Omega \rightarrow 1.5\omega_1$, where ω_1 is the first natural frequency of the beam for $s = s_0$. The sweep rate was set at $\Delta\Omega = 10$ Hz. This is achieved by incrementing the excitation frequency during each time step by a fixed amount keeping the force at a constant value. The second curve indicates the length of the unstuck beam when the excitation frequency is swept down: $1.5\omega_1 \rightarrow \Omega \rightarrow 0.1\omega_1$. Again the sweep rate was set to $\Delta\Omega = 10$ Hz. It is observed that sweeping the excitation frequency down produces complete repair while sweeping up only repairs the beam partially. This phenomenon is exactly the same as was observed in the preliminary experiments [20].

This behavior can be explained by understanding the shift in the first fundamental frequency ω_1 of the unstuck beam. As the beam begins to peel off $s(t)$ increases, and ω_1 begins to drop. As the excitation frequency is also decreased in the sweep down, bringing the excitation frequency Ω in closer proximity to ω_1. In a sense, the excitation chases the resonant frequency encouraging resonance and promoting repair. When the excitation frequency is swept up from $\Omega = 1.5\omega_1$ to $0.1\omega_1$ the excitation frequency increases while the natural frequency decreases. They quickly pass through one another and continue to move apart, preventing a continued near resonant condition and hindering the repair. It can be concluded that sweeping the excitation frequency down is more effective (i.e., down sweeps promote a more complete repair) than frequency sweep up.

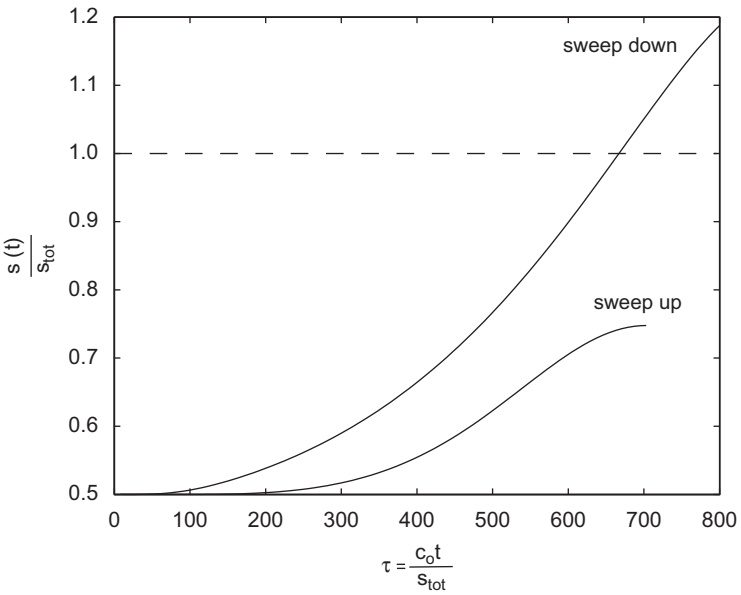

Fig. 6. A plot of non-dimensional beam length versus non-dimensional time showing the effect of frequency sweep up and down for a fixed force value. $s_0 = 500\,\mu$m, $s_{tot} = 1000\,\mu$m.

4.2.4. Frequency tracking

From the last section it is evident that there is a considerable advantage in sweeping the excitation frequency from a higher value to a lower value. The proximity of the excitation frequency to the resonant frequency and the transition for excitation frequency from super resonant to a sub-resonant region and vice versa has a profound effect on the extent of repair. This suggests that if the excitation frequency could be maintained near a resonant frequency at every instant then one could ensure a complete repair.

Fig. 7 shows the effects of frequency tracking. One curve shows the change in the unstuck length of the beam at a constant excitation frequency ratio of $\Omega = 0.9\omega_1$ where ω_1 is the first natural frequency for $s = s_0$ at a constant force amplitude of $P = 2000\,\mu$N. As explained in Section 4.2.2 the excitation is initially sub-resonant (though nearly resonant) and quickly changes to super-resonant, thus reducing the steady-state amplitude. The second curve represents the frequency case where $\Omega/\omega_i = 0.9$ is fixed. Here the ω_i is the time varying first natural frequency at every instant. The excitation frequency always remains sub-resonant (though nearly resonant). This process of maintaining a fixed ratio of Ω/ω_1 is referred to a frequency tracking, i.e., the excitation frequency tracks the resonant frequency. Note that a physical implementation of frequency tracking would require both sensing of the unstuck length (to monitor ω_i) and control to change Ω continuously. This would obviously create more experimental challenges than say, the frequency sweep approach where $\Delta\Omega$ is prescribed a priori. However, implementing this in a theoretical model is trivial; at every time step Ω is simply set to ω_i. From the two curves it can be clearly seen that there is at least 20% more repair for the case where the excitation frequency continuously tracks the first fundamental frequency.

4.2.5. Repair status

The previous sections concentrated on understanding the phenomenon associated with the repair process. The current section makes an effort to map the repair status in terms of a fixed force P and a fixed excitation frequency Ω. This does not include frequency sweeps or frequency tracking.

Fig. 8 represents a grid of data points which indicate either a partial repair (dots) or a complete repair (asterisks) as predicted by the model. The numerical simulations were performed by choosing each value of forcing amplitude and excitation frequency, and allowing the time integration to run forward from zero ICs. The simulation was stopped once $\dot{s} \leq 0$ and the unstuck length of the beam was recorded. The boundary (which has been sketched in) represents the separation of the two types of repair (partial versus complete) for the given forcing amplitude and excitation frequency. This grid is coarse and, hence, the boundary is not an exact demarcation of the two regions. Nonetheless, it serves as a guide for selecting force and excitation frequency values which will effect complete repair for the stiction failed microcantilevers.

This reconfirms the results presented earlier. At low frequencies, as large forcing amplitude is required to effect a complete repair. At slightly higher frequencies the force level is reduced (to a minimum around $\Omega/\omega_1 = 0.5$). It increases

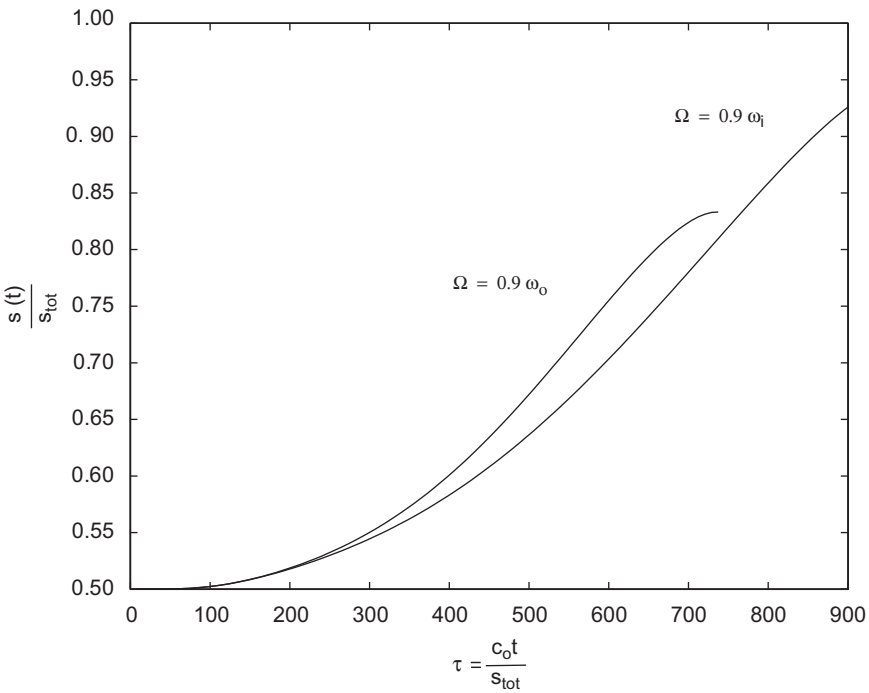

Fig. 7. A plot of non-dimensional beam length versus non-dimensional time showing the effect of frequency tracking for a fixed force value. $s_0 = 500\,\mu$m, $s_{tot} = 1000\,\mu$m.

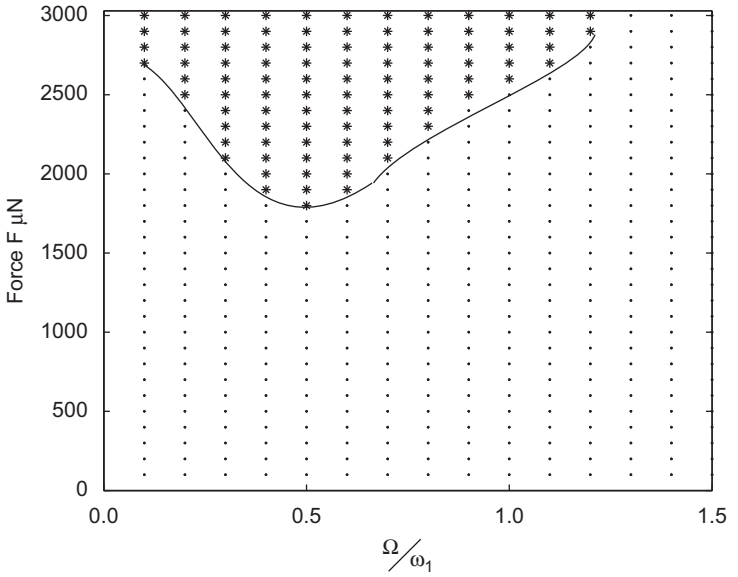

Fig. 8. A plot of forcing amplitude P versus frequency ratio of Ω/ω_1 showing partial dots and complete asterisk repair of a stiction failed microelectromechanical system cantilever beam. $s_0 = 500\,\mu\text{m}$, $s_{\text{tot}} = 1000\,\mu\text{m}$.

thereafter or higher frequencies near $\Omega/\omega_1 = 0.5$, debonding is initiated and the system gradually moves towards resonance as ω_1 decreases promoting complete repair. For frequencies well below or well above ω_1, the system does not spend enough time near a resonance condition to promote large amplitude vibration and complete repair.

5. Concluding remarks

This paper explores the physics of the dynamic debonding process for beams using a mechanical harmonic loading. The analytical modal incorporates dynamic fracture mechanics along with the dynamic modal amplitudes to capture the physics of stiction repair process. Numerical integration of the governing equation of motion is used to obtain a variety of results which give valuable insight to the influence of the forcing amplitude P and the excitation frequency Ω on the repair process. The effect of increasing the forcing amplitude is intuitive; increasing the force amplitude increases the extent of repair at a fixed frequency. The same cannot be said about the excitation frequency. The results show that the proximity of the excitation frequency to the natural frequency which changes as it begins to peel (changes as debonding proceeds) is critical. It is shown that exciting the beam at half of the first resonant frequency (of the beam with an initial unstuck length s_0) is most advantageous as the natural frequency drops as the beam debonds. Other physical processes for debonding (including frequency sweeps and frequency tracking) use their insight to promote more complete repair. Experimental results [20] confirm their general conclusions.

Appendix A. Constants used for numerical results

Below is a list of constants and their values that have been used in Eqs. (16)–(19):

$$C_1 = 0.3426\delta^2\rho A_r,$$

$$C_2 = 4.05125\rho A_r,$$

$$C_3 = 1.4492\delta\rho A_r,$$

$$C_4 = 0.5\rho A_r,$$

$$C_5 = 0.5371\delta\rho A_r,$$

$$C_6 = 0,$$

$$C_7 = 2.02725\rho A_r,$$

$$C_8 = 2.1732\rho A_r,$$

$$C_9 = 0.171\rho A_r,$$

$$C_{10} = 8.1025\rho A_r,$$

$$C_{11} = 1.4492\delta\rho A_r,$$

$$P_1 = 0.00085EI\delta,$$

$$P_2 = 18EI\delta^2,$$

$$P_3 = 752EI,$$

$$P_4 = 0.5\rho A_r,$$

$$P_5 = 0.5371\delta,$$

$$P_6 = 1.00\rho A_r,$$

$$P_7 = 4.06\rho A_r,$$

$$P_8 = 0.726\delta\rho A_r,$$

$$P_9 = -1.0\rho A_r,$$

$$P_{10} = 500EI,$$

$$P_{11} = 0.000286EI\delta,$$

where $\rho = 2331\,\mathrm{kg/m^3}$, $A_r = b \times h$, $b = 30 \times 10^{-6}\,\mathrm{m}$, $b = 2 \times 10^{-6}\,\mathrm{m}$, $\delta = 2 \times 10^{-6}\,\mathrm{m}$, $E = 160 \times 10^9\,\mathrm{N/m^2}$, $I = bh^3$.

References

[1] W. Merlijn van Spengen, MEMS reliability from a failure mechanisms perspective, *Microelectronics Reliability* 43 (7) (2003) 1049–1060.
[2] W. Merlijn van Spengen, R. Puers, I. De Wolf, A physical model to predict stiction in MEMS, *Journal of Micromechanics and Microengineering* 12 (2002) 702–713.
[3] C.H. Mastrangelo, C.H. Hsu, Mechanical stability and adhesion of microstructures under capillary forces. Part I. Basic theory, *Journal of Microelectromechanical Systems* 2 (1993) 33–43.
[4] C.H. Mastrangelo, C.H. Hsu, Mechanical stability and adhesion of microstructures under capillary forces. Part II. Experiments, *Journal of Microelectromechanical Systems* 2 (1993) 44–55.
[5] M.P. de Boer, J.A. Knapp, T.A. Michalske, U. Srinivasan, R. Maboudian, Adhesion hysteresis of silane coated microcantilevers, *Acta Materialia* 48 (2000) 4531–4541.
[6] R.W. Johnstone, M. Parameswaran, Theoretical limits on the freestanding length of cantilevers produced by surface micromachining technology, *Journal of Micromechanics and Microengineering* 12 (2002) 855–861.
[7] D. Nilsson, S. Jensen, A. Menon, Fabrication of silicon molds for polymer optics, *Journal of Micromechanics and Microengineering* 13 (2003) S57–S61.
[8] W.R. Ashurst, C. Yau, C. Carraro, C. Lee, G.J. Kluth, T.R. Howe, R. Maboudian, Alkene based monolayer films as anti-stiction coatings for polysilicon MEMS, *Sensors and Actuators A—Physical* 91 (3) (2001) 239–248.
[9] J.K. Luo, Y.Q. Fu, H.R. Le, J.A. Williams, S.M. Spearing, W.I. Milne, Diamond and diamond-like carbon coatings MEMS, *Journal of Micromechanics and Microengineering* 17 (2007) S147–S163.
[10] N.C. Tien, S. Jeong, L.M. Phinney, K. Fushinobu, J. Bokor, Surface adhesion reduction in silicon microstructures using femotosecond laser pulses, *Applied Physics Letters* 66 (2) (1995) 197–199.
[11] K. Fushinobu, L.M. Phinney, N.C. Tien, Ultrashort-pulse laser heating of silicon to reduce microstructure adhesion, *International Journal of Heat and Mass Transfer* 39 (15) (1996) 3181–3186.
[12] L.M. Phinney, J.W. Rogers, Pulsed laser repair of adhered surface-micromachined polycrystalline silicon cantilevers, *Journal of Adhesion Science and Technology* 17 (4) (2003) 603–622.
[13] V. Gupta, R. Snow, M. Wu, A. Jain, J. Tsai, Recovery of stiction-failed MEMS structures using laser induced stress waves, *Journal of Microelectromechanical Systems* 13 (4) (2004) 696–700.
[14] Z.C. Leseman, S. Koppaka, T.J. Mackin, A fracture mechanics description of stress wave repair in stiction-failed microcantilevers: theory and experiments, *Journal of Microelectromechanical Systems* 16 (4) (2007) 904–911.
[15] M.P. de Boer, D.L. Luck, W.R. Ashurst, R. Maboudian, A.D. Corwin, J.A. Walraven, J.M. Redmond, High performance surface micromachined inchworm actuator, *Journal of Microelectromechanical Systems* 13 (1) (2004) 63–74.
[16] W. Merlijn van Spengen, R. Puers, R. Mertens, I. De Wolf, A low frequency electrical test set-up for the reliability assessment of capacitive RF MEMS switches, *Journal of Micromechanics and Microengineering* 13 (2003) 604–612.
[17] D. Dubuc, M. Saddaoui, S. Melle, F. Flourens, L. Rabbia, B. Ducarouge, K. Grenier, P. Pons, A. Boukabache, L. Bary, A. Takacs, H. Aubert, O. Vendier, J.L. Roux, R. Plana, Smart MEMS concept for high secure RF and millimeterwave communications, *Microelectronics Reliability* 44 (2004) 899–907.
[18] U. Srinivasan, M.R. Houston, R.T. Howe, R. Maboudian, Alkyltrichlorosilane-based self assembled monolayer films for stiction reduction in silicon micromachines, *Journal of Microelectromechanical Systems* 7 (2) (1998) 252–260.
[19] N. Tas, T. Sonnenberg, H. Jansen, R. Legtenberg, M. Elwenspoek, Stiction in surface micromachining, *Journal of Micromechanics and Microengineering* 6 (1996) 385–397.
[20] A.A. Savkar, K.D. Murphy, Z.C. Leseman, T.J. Mackin, M.R. Begley, On the use of structural vibrations to release stiction failed MEMS, *Journal of Microelectromechanical Systems* 16 (1) (2007) 163–173.
[21] A.A. Savkar, A Study of Stiction Repair in Micro-Cantilevers Using Structural Vibrations, Ph.D. Thesis, The University of Connecticut, Storrs, CT, 2007.
[22] L.B. Freund, *Dynamic Fracture Mechanics*, Cambridge University Press, Cambridge, 1990.
[23] J.P. Berry, Some kinetic consideration of the Griffith criterion for fracture—I, Equation of motion at constant force, *Journal of the Mechanics and Physics of Solids* 8 (1960) 194–206.

[24] M.F. Kanninen, An augmented double cantilever beam model for studying crack propagation and arrest, *International Jouranl of Fracture* 9 (1) (1973) 83–91.
[25] M.F. Kanninen, A dynamic analysis of unstable crack propagaion and arrest in DCB test specimen, *International Journal of Fracture* 10 (3) (1974) 415–430.
[26] C.T. Chang, R.C. Craig, Normal modes of uniform beams, *Journal of Engineering Mechanics Division, ASCE* (1969) 1027–1031.
[27] W.D. Zhu, J. Ni, Energetics and stability of translating media with an arbitrary varying length, *Journal of Vibration and Acoustics* 122 (2000) 295–304.
[28] W.H. Press, W.T. Vetterling, S.A. Teukolsky, B.P. Flannery, *Numerical Recipes in Fortran: The Art of Scientific Computing*, Cambridge University Press, New York, 1994.